SENSITIVITY STUDIES ON THE CALCULATION OF THE RADIATION BALANCE OF URBAN SURFACES: II. LONGWAVE RADIATION

D. L. VERSEGHY* and D. S. MUNRO

Department of Geography, University of Toronto, Erindale Campus, Mississauga, Ontario, L5L 1C6, Canada

(Received 2 September, 1988)

Abstract. The model developed in Verseghy and Munro (1989) is extended to the calculation of the longwave radiation incident on building surfaces. When compared with field measurements, the average magnitude of error associated with model predictions is found to be 10 W m^{-2}. The effects of six simplifying assumptions are investigated. The neglect of horizon obstructions is found to lead to errors of up to 60 W m^{-2}; the assumption of wall temperatures equal to air temperatures results in errors of up to 35 W m^{-2}. The neglect of absorption and emission by air between pairs of walls causes errors of the same magnitude as those associated with the predictions of the rigorous model itself. Of the three remaining simplifying assumptions tested (the assumption of isotropic sky radiation, the use of published values of emissivities instead of measured values, and the blackbody surface assumption), none results in errors >5 W m^{-2}. As in the shortwave case, the errors are site-specific, but nevertheless indicate the care with which the use of simplifying assumptions must be approached.

1. Introduction

In a recent paper, Verseghy and Munro (1989) dealt with the shortwave radiation incident on building surfaces. Of similar importance in the field of urban climatology is the incoming longwave radiation, singled out by Oke (1982) as being possibly the most important factor influencing the development of the urban heat island. However, the modelling of incident longwave radiation for building surfaces is even more involved than that of shortwave radiation. The calculation must in both cases incorporate the radiative properties and locations of the surfaces viewed, and the effects of sky anisotropy; for longwave radiation, however, the temperatures of the viewed surfaces and the attenuation of radiation by air between pairs of walls must also be taken into account. Individual studies exist attesting to the importance of these factors. Siegel and Howell (1981) reported that measured emissivities of building materials may differ from tabulated values by up to 0.60, due to aging effects; Kondratyev (1969) calculated that the thickness of the atmospheric layer which generates 99% of the incoming radiation received at the earth's surface varies between approximately 4 km within the atmospheric window and 1 km for the rest of the longwave spectrum. Studies which relate specifically to urban areas tend to be theoretical

* Current affiliation: Atmospheric Environment Service, 4905 Dufferin St., Downsview, Ontario, M3H 5T4, Canada.

Boundary-Layer Meteorology **48**: 1–18, 1989.

in nature and unsubstantiated by field measurements; however, some indication can be gleaned as to possible magnitudes of errors associated with simplifying assumptions. Cole (1979) estimated that assuming incoming longwave radiation to include only isotropically-distributed sky radiation may lead to errors of greater than 30 W m^{-2} for vertical surfaces. Sutherland and Bartholic (1972), and Arnfield (1976) demonstrated the effects of longwave radiation trapping in row crops and urban canyons, respectively. Finally, Todhunter and Terjung (1988) concluded that models which incorporate varying degrees of complexity in radiation geometry may differ in their predictions of the net longwave radiation of buildings by up to 75 W m^{-2}.

Because of the complexity of the urban radiation field, an evaluation from first principles of the longwave radiation incident on urban surfaces must clearly present even more difficulties than that of incident shortwave radiation. A comparison of the results of a rigorous, field-tested model with those of versions which neglect the factors listed above therefore seems of particular value. This paper describes an extension of the work on shortwave radiation presented in Verseghy and Munro (1989), and its application to the longwave radiation case.

2. The Model

As in our earlier paper, a building courtyard was selected for study, in order to simplify the problem of instrumentation. A description of the radiation enclosure theory used in constructing the model, and an outline of the calculation of input parameters, are given below. Additional details relating to the model can be found in Verseghy (1987).

The longwave radiosity $J_{L,i}$ of a surface i comprises not only the radiation reflected from the surface, but also that emitted by it:

$$J_{L,i} = \epsilon_i \sigma T_i^4 + (1 - \epsilon_i) G_{L,i} \tag{1}$$

where ϵ_i represents the longwave emissivity of surface i, T_i its temperature and $G_{L,i}$ the incoming longwave flux density. (The assumption that the longwave reflectivity is equal to $(1 - \epsilon_i)$ will be discussed in the next section.) $G_{L,i}$ is derived from three sources: sky emission; radiation transmitted through the air from the N other surfaces which the wall sees; and emission by the air intervening between pairs of walls. Thus,

$$G_{L,i} = \sum_{j=1}^{N} [\tau_{a,ij} J_{L,j} + \epsilon_{a,ij} \sigma T_a^4] F_{ij} + G_{L,is} \tag{2}$$

where $\tau_{a,ij}$ and $\epsilon_{a,ij}$ are the average atmospheric transmissivity and emissivity over the path between walls i and j, T_a is the air temperature, F_{ij} is the view factor from wall i to wall j, and $G_{L,is}$ is the longwave radiation from the sky.

Substituting Equation (2) into Equation (1) and rearranging results in

$$J_{L,i} - (1 - \epsilon_i) \sum_{j=1}^{N} \tau_{a,ij} F_{ij} J_{L,j}$$

$$= \epsilon_i \sigma T_i^4 + (1 - \epsilon_i) \left[\sigma T_a^4 \sum_{j=1}^{N} \epsilon_{a,ij} F_{ij} + G_{L,is} \right]. \tag{3}$$

As in the shortwave radiation case, a system of linear equations results, of the form

$$\sum_{j=1}^{N} a_{ij} J_{L,j} = c_i \,. \tag{4}$$

Here, the constants a_{ij} and c_i are given by the relations

$$a_{ij} = \delta_{ij} - (1 - \epsilon_i) \tau_{a,ij} F_{ij} \tag{5}$$

where δ_{ij} represents the Kronecker delta, and

$$c_i = \epsilon_i \sigma T_i^4 + (1 - \epsilon_i) \left[\sigma T_a^4 \sum_{j=1}^{N} \epsilon_{a,ij} F_{ij} + G_{L,is} \right] \tag{6}$$

respectively. If the terms on the right sides of Equations (5) and (6) are known, therefore, the vector of unknown radiosities can be evaluated as in Verseghy and Munro (1989) using the Gauss–Jordan technique. The incoming longwave radiation terms $G_{L,i}$ can then be obtained by solving Equation (1) for each wall.

The data required to solve Equations (5) and (6) include the terms ϵ_i, T_i, T_a, $\epsilon_{a,ij} F_{ij}$, $\tau_{a,ij} F_{ij}$ and $G_{L,is}$. ϵ_i, T_i and T_a are obtained from field measurements; the evaluation of the remaining terms is outlined below.

The atmospheric emissivity between two surfaces is a function of the path length L between them and the concentration of emitting gases. Since the path length varies among pairs of incremental areas of two walls, the atmospheric emissivity must be weighted with respect to L. This can most efficiently be accomplished by combining the calculation with that of F_{ij}:

$$\epsilon_{a,ij} F_{ij} = \frac{1}{A_i} \int_{A_j} \int_{A_i} \frac{\epsilon_a(L) \cos \theta_i \cos \theta_j}{\pi L^2} \cdot \mathrm{d}A_i \cdot \mathrm{d}A_j \tag{7}$$

where $\epsilon_a(L)$ is the emissivity along the path length L, θ_i and θ_j are the angles made by the line L with the normals to the incremental areas $\mathrm{d}A_i$ and $\mathrm{d}A_j$, and A_i and A_j are the areas of the two walls. $\epsilon_a(L)$ is calculated as the sum of the emissivities of water vapour $\epsilon_w(L)$ and carbon dioxide $\epsilon_c(L)$ integrated over the path length, minus a correction term $\epsilon_\delta(L)$ to account for overlap in the wings of the water vapour and carbon dioxide emission bands:

$$\epsilon_a(L) = \epsilon_w(L) + \epsilon_c(L) - \epsilon_d(L) \,. \tag{8}$$

The three terms on the right are tabulated as functions of temperature and optical depth by Staley and Jurica (1970). The optical depths of water vapour and carbon dioxide are easily calculated over the path length if their concentrations are known.

Since scattering can be neglected for longwave radiation, the sum of the atmospheric transmissivity and absorptivity over the path length is effectively unity. If the radiation emitted by the walls is assumed to be diffuse gray in nature, and if most of the walls in the enclosure can be assumed to be shaded and therefore relatively close to the air temperature, the atmospheric absorptivity can be approximated by the emissivity. Thus,

$$\tau_a(L) = 1 - \epsilon_a(L) . \tag{9}$$

The calculation of $\tau_{a,ij}F_{ij}$ can then be carried out by means of an equation analogous to (7):

$$\tau_{a,ij}F_{ij} = \frac{1}{A_i} \int_{A_j} \int_{A_i} \frac{[1 - \epsilon_a(L)] \cos \theta_i \cos \theta_j}{\pi L^2} \cdot dA_i \cdot dA_j . \tag{10}$$

The longwave sky radiance $G'_{L,s}(\theta)$ varies with u, the depth of precipitable water, and the secant of the zenith angle θ. The equation presented by Unsworth and Monteith (1975) for the angular distribution of $G'_{L,s}(\theta)$ is of the form

$$G'_{L,s}(\theta) = p + q[\ln(u \cdot \sec \theta)] \tag{11}$$

where p and q are constants. (Other researchers, e.g., Martin and Berdahl (1984), have used an exponential variation of sec θ, which produces an almost identical fit up to angles of 60°, but Equation (11) is preferred as being better supported by field measurements.) Making use of logarithm identities, (11) can be rewritten in terms of $G'_{L,s}(0)$ as

$$G'_{L,s}(\theta) = G'_{L,s}(0)[1 + r \cdot \ln(\sec \theta)] \tag{12}$$

where r is a constant. The value of r can be determined by integrating Equation (12) over θ to obtain the longwave sky irradiance $G_{L,hs}$ for a flat surface h with an unobstructed horizon. An equation results relating r to the ratio between $\pi G'_{L,s}(0)$ and $G_{L,hs}$:

$$r = \frac{1 - [\pi G'_{L,s}(0)/G_{L,hs}]}{0.5 \cdot [\pi G'_{L,s}(0)/G_{L,hs}]} . \tag{13}$$

To find $G_{L,is}$ for each wall i, Equation (12) must be integrated over the portion of sky viewed and over the wall subareas dA_i:

$$G_{L,is} = \int_{A_i} \int_{\phi_1}^{\phi_2} \int_{0}^{\theta(\phi)} G'_{L,s}(\theta) \cdot \cos \theta_i \sin \theta \cdot d\theta \cdot d\phi \cdot dA_i \tag{14}$$

where ϕ_1 and ϕ_2 represent the azimuth angles bounding the sector of sky viewed by the wall, $\theta(\phi)$ the local horizon angle at azimuth angle ϕ, and θ_i the angle which radiation from the sky increment in question makes with the normal to the surface. The calculation of $G_{L,is}$ can be simplified by a method analogous to that used in the determination of the overcast sky diffuse radiation in Verseghy and Munro (1989), i.e., by partitioning the sky into N narrow zenithal annuli between 0° and 90° and finding the sum of the products of the view factor $F_{is}(\Delta\theta)$ of each annulus and $G'_{L,s}(\theta)$ evaluated at the midpoint of that annulus:

$$G_{L,is} = \sum_{k=1}^{N} G'_{L,s}(\theta) F_{is}(\Delta\theta) . \tag{15}$$

The $F_{is}(\Delta\theta)$ terms are calculated as in Verseghy and Munro (1989) from

$$F_{is}(\Delta\theta) = \int_{A_i} \int_{\phi_1}^{\phi_2} \int_{\theta_1}^{\theta_2} \cos\theta_i \sin\theta \cdot d\theta \cdot d\phi \cdot dA_i \tag{16}$$

where θ_1 and θ_2 represent the zenithal boundaries of each annulus.

3. Field Measurements

The sites, wall subareas defined and measurement days were the same as those described in our earlier paper. For each wall subarea, the emissivity was calculated as a weighted average over the building materials present. Emissivities of building materials were measured *in situ* (except in the case of the roof tiles at site 2). This was accomplished by using a Barnes PRT-5 narrow-view radiometer in conjunction with an "emissivity box" of the type described by Buettner and Kern (1965). For details, see Verseghy (1987). A summary of the results is given in Table I, together with values taken from the literature for comparison.

Strictly speaking, the emissivity ϵ_i and longwave absorptivity $\alpha_{L,i}$ of a surface are, like its shortwave reflectivity, functions of wavelength λ, angles of incidence θ and ϕ, and surface temperature T_i. The general form of Kirchhoff's law states

$$\epsilon_i(\lambda, \theta, \phi, T_i) = \alpha_{L,i}(\lambda, \theta, \phi, T_i) ; \tag{17}$$

the absorptivity and longwave reflectivity $\rho_{L,i}$ for opaque materials are related by

$$\alpha_{L,i}(\lambda, \theta, \phi, T_i) + \rho_{L,i}(\lambda, \theta, \phi, T_i) = 1 . \tag{18}$$

The wavelength and temperature dependence can be neglected over the range of terrestrial values. Moreover, since the roughness of the surfaces studied was in general large compared to the wavelength of longwave radiation, the surfaces could be considered, as in the shortwave case, to behave as diffuse reflectors. The only exception was in the case of glass, which being smooth with respect to shortwave radiation was *ipso facto* even smoother with respect to longwave

TABLE I

Longwave emissivities for enclosure surfaces. (Literature values from ASHRAE, 1977; Siegel and Howell, 1981; Sellers, 1965; Oke, 1978)

	Surface	Measured ϵ	Literature ϵ
Site #1	Stucco	0.98	0.90
	Ordinary windows	0.98	0.90
	Brown brick	0.96	0.92
	Light brown tile	0.98	0.90
	Green painted door	0.97	0.90
Site #2	Light gray stone	0.93	0.92
	Dark gray stone	0.93	0.92
	Green roof tile	–	0.90
	Leaded-glass windows	0.93	0.90
	Varnished oak door	0.95	0.90
	Green lawn	0.95	0.95
	Asphalt	0.94	0.94

radiation, and therefore produced specular reflections, with reflectivities increasing greatly in magnitude at grazing angles. However, since the longwave reflectivity of glass averaged hemispherically is less than 0.10, and the distribution of incoming longwave radiation in a building enclosure can be considered as approximately isotropic, specular reflections were neglected, and the value of direct normal reflectivity measured at each site was assumed to approximate the total hemispherical reflectivity. Thus, the spectral, angular and thermal dependencies of the longwave reflectivity, and therefore of the longwave absorptivity and emissivity of the surfaces studied were ignored. Omitting the notations of functional dependence for ϵ_i, $\rho_{L,i}$ and $\alpha_{L,i}$, and combining Equations (17) and (18) results in

$$\epsilon_i + \rho_{L,i} = 1 , \tag{19}$$

which is the relation assumed in the derivation of Equation (1).

As in the shortwave radiation study, measurements were made at rooftop level, at one or two test walls, and on the ground within the enclosure. Swissteco net radiometers were converted to one-sided instruments by fitting one hemisphere with a black-body cap whose temperature was monitored by a thermocouple. The polythene domes of the instruments were kept inflated by air pumped through a dessicant. Each instrument was paired with a Kipp–Zonen pyranometer; the incoming shortwave radiation measured by the latter was subtracted from the total incoming radiation given by the former to yield the incoming longwave radiation. One pair of instruments was placed on the tallest structure adjacent to the enclosure, to measure the sky longwave radiation $G_{L,hs}$ incident on an unobstructed horizontal surface; others were mounted on selected wall subareas

to test model predictions of $G_{L,i}$. Ambient air temperature was measured at the floor of the enclosure by a shaded thermocouple. All of the above measurements were collected by a data logger and recorded as 5-min averages, based on scans made every 15 s.

The evaluation of the surface temperatures of wall subareas was carried out at the floor of the enclosure using the Barnes PRT-5 narrow-view radiometer, which produced values corresponding to effective black-body temperature. The latter was assumed to differ by a negligible amount from the actual surface temperature, since the emissivities of all surfaces were high, and at least half of the reflected radiation generally originated from surfaces whose temperature was relatively close to that of the subarea in question. Scans of the surfaces within the enclosure were made every half hour. Sky longwave radiation from the zenith, $G'_{L,s}(0)$, was measured on cloudy days twice every half hour, using an upward-pointing narrow-view Linke–Feussner radiometer; on clear days, the radiance proved too weak for measurement, so a constant value of 0.95 was chosen for the ratio $\pi G'_{L,s}(0)/G_{L,hs}$, based on measurements reported by Kondratyev (1969).

4. Results and Discussion

The same twelve wall subareas were selected for in-depth study as in Verseghy and Munro (1989): i.e., the north, east, south and west faces of the first and fourth floors at site 1, and the centre subareas of the four walls at site 2. The sky, ground and wall view factors of the subareas are reproduced in Table II.

The predictions of incoming longwave radiation made by the rigorous model were first tested against field measurements, for the same one or two wall subareas at each site as in our earlier paper. Mean bias and root-mean-square errors are presented in Table III, and the diurnal variations of observed and predicted incoming radiation are illustrated for four sample subareas in Figure 1. It is evident that errors are smallest when the instruments view mainly shaded walls and/or when sky conditions are overcast; errors are greatest when neither

TABLE II

Totalled sky, ground and wall view factors for test walls

		Sky	Ground	Walls
Site #1	Upper N, S walls	0.34	0.09	0.57
	Upper E, W walls	0.35	0.09	0.56
	Lower N, S walls	0.09	0.34	0.57
	Lower E, W walls	0.09	0.35	0.56
Site #2	N wall	0.35	0.42	0.23
	E wall	0.33	0.45	0.22
	S wall	0.40	0.36	0.24
	W wall	0.34	0.43	0.23

TABLE III

Statistical description of prediction errors of rigorous model (Units of W m^{-2})

	Wall	Day	Average prediction	Mean bias error	Rms error
Site #1	Lower east	1 (Clear)	311.7	3.2	5.4
	Upper east	2 (Cloudy)	325.3	−8.3	11.4
	Upper east	3 (Clear)	330.2	−14.0	21.3
	Lower west	1 (Clear)	311.9	2.5	6.5
	Lower west	2 (Cloudy)	343.6	−3.5	7.9
	Middle west	3 (Clear)	354.3	−6.4	13.4
Site #2	West	1 (Clear)	388.6	9.5	15.4
	West	2 (Clear)	369.3	−7.5	17.9
	West	3 (Cloudy)	428.0	3.9	12.7

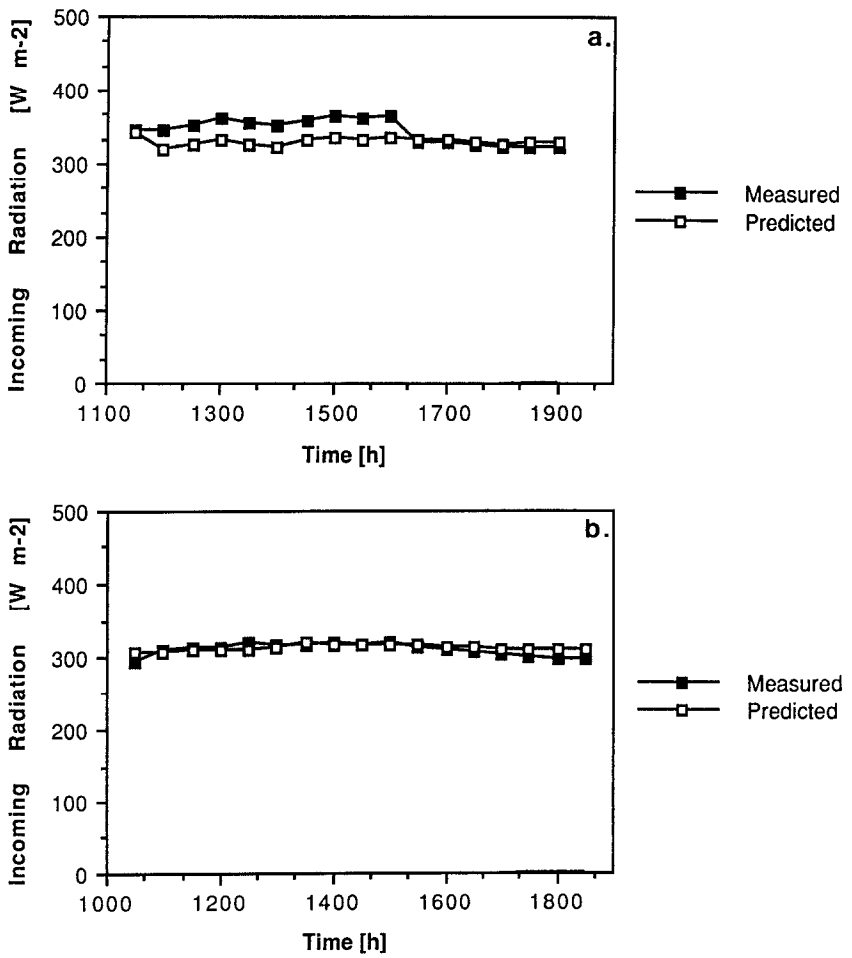

Fig. 1. Diurnal variation of measured and predicted incoming longwave radiation. (a) Site #1, upper east wall: day 3, (b) Site #1, lower west wall: day 1.

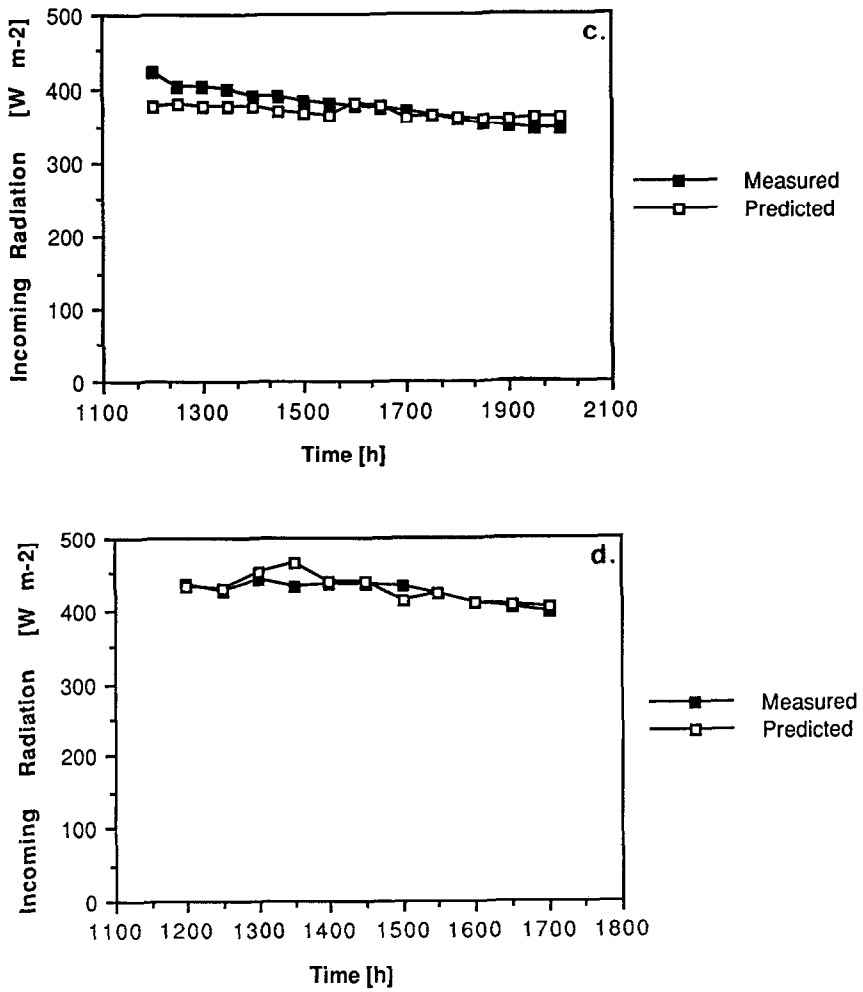

Fig. 1 (continued). Diurnal variation of measured and predicted incoming longwave radiation. (c) Site #2, west wall: day 2, (d) Site #2, west wall: day 3.

condition holds, i.e., for the upper east wall at site 1 on day 3, and for the first two days at site 2. The improvement in the prediction in the former case is quite marked when the enclosure falls into shade at 1630 h. The larger error associated with sunlit conditions can be attributed to the fact that only one "sunny" and one "shady" temperature measurement were made for each wall subarea. For subareas three storeys tall, as at site 2, or where the illuminated fraction was changing rapidly, the measured temperatures may not have been representative of the area in question. Moreover, the assumption that the effective blackbody temperature measured by the Barnes radiometer was equal to the actual surface

temperature might have introduced errors as well, particularly for the upper wall subareas at site 1. The temperature of these was measured from ground level, at the angle of approximately 60° to the normal; at such large angles, given the relatively smooth surface of stucco, specular reflections of sky radiation may have occurred, leading to an underestimation of the actual surface temperature. As an example, a wall at a temperature of 15 °C and with a directional reflectivity of 0.10 at 60° from the normal, which viewed a sky radiating at 230 W m^{-2}, would appear from below to radiate as a black body at 12 °C. If better care is taken in measuring surface temperatures, however, it can be concluded that on the whole, the root-mean-square errors associated with the predictions of the rigorous model should be of the order of 10 W m^{-2}.

As in our earlier paper, the model was then run incorporating various simplifying assumptions. The same days of meteorological data were used as input for the runs, i.e., days 1 and 2 at sites 1 and 2, respectively, for clear skies, and days 2 and 3 at sites 1 and 2, respectively, for cloudy skies. Six simplifications were modelled: the neglect of horizon obstructions, the assumption of isotropic sky radiation, the neglect of air in the enclosure, the assumption that wall and ground temperatures equalled air temperatures, the use of published values of emissivities, and the modelling of all surfaces as black bodies. Mean bias and root-mean-square errors for all the walls under study are listed in Tables IV and V for clear and cloudy conditions, respectively. It will be noted that variations in the magnitude of error among walls of different orientations at a given height are much smaller than in the case of clear-sky shortwave radiation; this is primarily a result of the fact that the angular distribution of sky longwave radiation, like that of diffuse radiation under overcast conditions, is independent of azimuth.

As in the shortwave case, the neglect of horizon obstructions produces the most serious errors. Figures 2 and 3 show the diurnal variations in prediction errors for selected walls under clear and cloudy conditions, respectively. The neglect of horizon obstructions involves replacing radiation received from warm walls with that from the colder sky; this leads to underestimation of incoming longwave radiation on all walls. The magnitude of error is greatest for the lower walls at site 1 due to their small sky view factors. Errors are also larger for clear skies than for overcast skies, since under cloudy conditions the wall-sky temperature difference is less. Thus, on the lower walls at site 1, underestimations average 60 W m^{-2} for clear skies and 36 W m^{-2} for overcast skies. On the upper walls at site 1, the average errors are 33 and 18 W m^{-2} under clear and cloudy skies, respectively, and for the walls at site 2, the clear-sky and cloudy-sky errors average 12 and 7 W m^{-2}, respectively. Variations in clear-sky errors among walls at the same height at a given site are caused by varying views of warm, sunlit walls. Underestimations are on the whole larger for the upper walls at site 1 than for the walls at site 2, even though their sky view factors are nearly equal, because of the times of year at which measurements were taken. Data were collected at site 1 during February and March, and at site 2 during April and

TABLE IV

Errors caused by simplifying assumptions for incoming longwave radiation under clear skies (Units of $W\ m^{-2}$)

	Rigorous model prediction	Clear horizon		Isotropic sky		Air $\tau = 1$	
		Mean bias	Rms error	Mean bias	Rms error	Mean bias	Rms error
North walls							
Lower, site #1	312.3	−58.8	58.9	0.4	0.4	8.7	8.8
Upper, site #1	283.3	−29.7	29.9	−1.4	1.4	7.4	7.6
Site #2	372.3	−17.1	21.5	−2.4	2.4	4.4	6.2
East walls							
Lower, site #1	312.0	−58.5	58.6	0.3	0.3	8.5	8.6
Upper, site #1	287.6	−34.1	34.2	−1.9	1.9	8.1	8.2
Site #2	363.8	−8.7	12.4	−1.6	1.6	2.6	3.9
South walls							
Lower, site #1	315.5	−61.9	62.1	0.4	0.4	10.0	10.0
Upper, site #1	289.0	−35.4	35.6	−1.4	1.4	9.7	9.7
Site #2	361.1	−6.0	7.5	−3.6	3.6	3.9	4.3
West walls							
Lower, site #1	312.3	−58.7	58.9	0.3	0.3	8.6	8.7
Upper, site #1	288.0	−34.4	34.6	−1.9	1.9	8.3	8.4
Site #2	369.3	−14.1	16.8	−1.6	1.6	3.5	4.3

	Rigorous model prediction	Wall T = air T		Literature ϵ		All blackbody	
		Mean bias	Rms error	Mean bias	Rms error	Mean bias	Rms error
North walls							
Lower, site #1	312.3	−29.3	29.5	−1.7	1.7	0.5	0.5
Upper, site #1	283.3	−22.3	22.7	−1.6	1.6	0.5	0.5
Site #2	372.3	−12.9	16.9	−0.3	0.4	2.1	2.4
East walls							
Lower, site #1	312.0	−29.8	30.0	−1.6	1.7	0.5	0.5
Upper, site #1	287.6	−25.7	25.9	−2.0	2.0	0.6	0.6
Site #2	363.8	−5.2	8.4	−0.1	0.1	1.6	1.7
South walls							
Lower, site #1	315.5	−32.3	32.4	−2.0	2.0	0.6	0.6
Upper, site #1	289.0	−28.0	28.1	−2.1	2.1	0.6	0.6
Site #2	361.1	−5.5	6.4	−0.1	0.2	1.4	1.5
West walls							
Lower, site #1	312.3	−30.1	30.3	−1.7	1.7	0.5	0.5
Upper, site #1	288.0	−26.1	26.3	−2.0	2.0	0.6	0.6
Site #2	369.3	−9.5	11.6	−0.1	0.2	1.9	2.0

TABLE V

Errors caused by simplifying assumptions for incoming longwave radiation under cloudy skies (Units of W m^{-2})

	Rigorous model prediction	Clear horizon		Isotropic sky		Air $\tau = 1$	
		Mean bias	Rms error	Mean bias	Rms error	Mean bias	Rms error
North walls							
Lower, site #1	345.1	−37.1	37.8	0.0	0.0	7.2	7.3
Upper, site #1	326.5	−18.5	18.7	0.0	0.0	3.7	3.7
Site #2	429.8	−8.9	10.2	−3.3	3.3	7.5	7.9
East walls							
Lower, site #1	343.5	−35.4	36.2	0.0	0.0	7.6	7.6
Upper, site #1	325.3	−17.2	17.4	0.0	0.0	5.6	5.6
Site #2	426.5	−5.6	7.9	−2.2	2.2	7.6	8.3
South walls							
Lower, site #1	345.6	−37.6	38.4	0.0	0.0	7.5	7.5
Upper, site #1	326.5	−18.5	18.6	0.0	0.0	4.6	4.6
Site #2	425.7	−4.7	6.0	−5.0	5.0	7.5	7.9
West walls							
Lower, site #1	343.6	−35.6	36.4	0.0	0.0	7.3	7.3
Upper, site #1	325.8	−17.7	17.9	0.0	0.0	4.9	4.9
Site #2	428.0	−7.1	8.8	−2.2	2.2	5.9	6.4

	Rigorous model prediction	Wall T = air T		Literature ϵ		All blackbody	
		Mean bias	Rms error	Mean bias	Rms error	Mean bias	Rms error
North walls							
Lower, site #1	345.1	−23.4	23.5	−1.2	1.2	0.4	0.4
Upper, site #1	326.5	−13.1	13.1	−0.8	0.8	0.2	0.2
Site #2	429.8	−14.7	15.6	−1.0	3.1	0.7	0.8
East walls							
Lower, site #1	343.5	−22.8	22.9	−1.1	1.1	0.3	0.3
Upper, site #1	325.3	−13.5	13.5	−0.8	0.9	0.3	0.3
Site #2	426.5	−13.0	14.5	−0.1	0.1	0.5	0.7
South walls							
Lower, site #1	345.6	−24.0	24.1	−1.3	1.3	0.4	0.4
Upper, site #1	326.5	−13.6	13.7	−0.8	0.8	0.2	0.2
Site #2	425.7	9.8	10.6	−0.1	0.1	0.4	0.5
West walls							
Lower, site #1	343.6	−22.8	22.8	−1.1	1.1	0.3	0.3
Upper, site #1	325.8	−13.5	13.5	−0.9	0.9	0.2	0.2
Site #2	428.0	−13.2	14.4	0.0	0.0	0.5	0.7

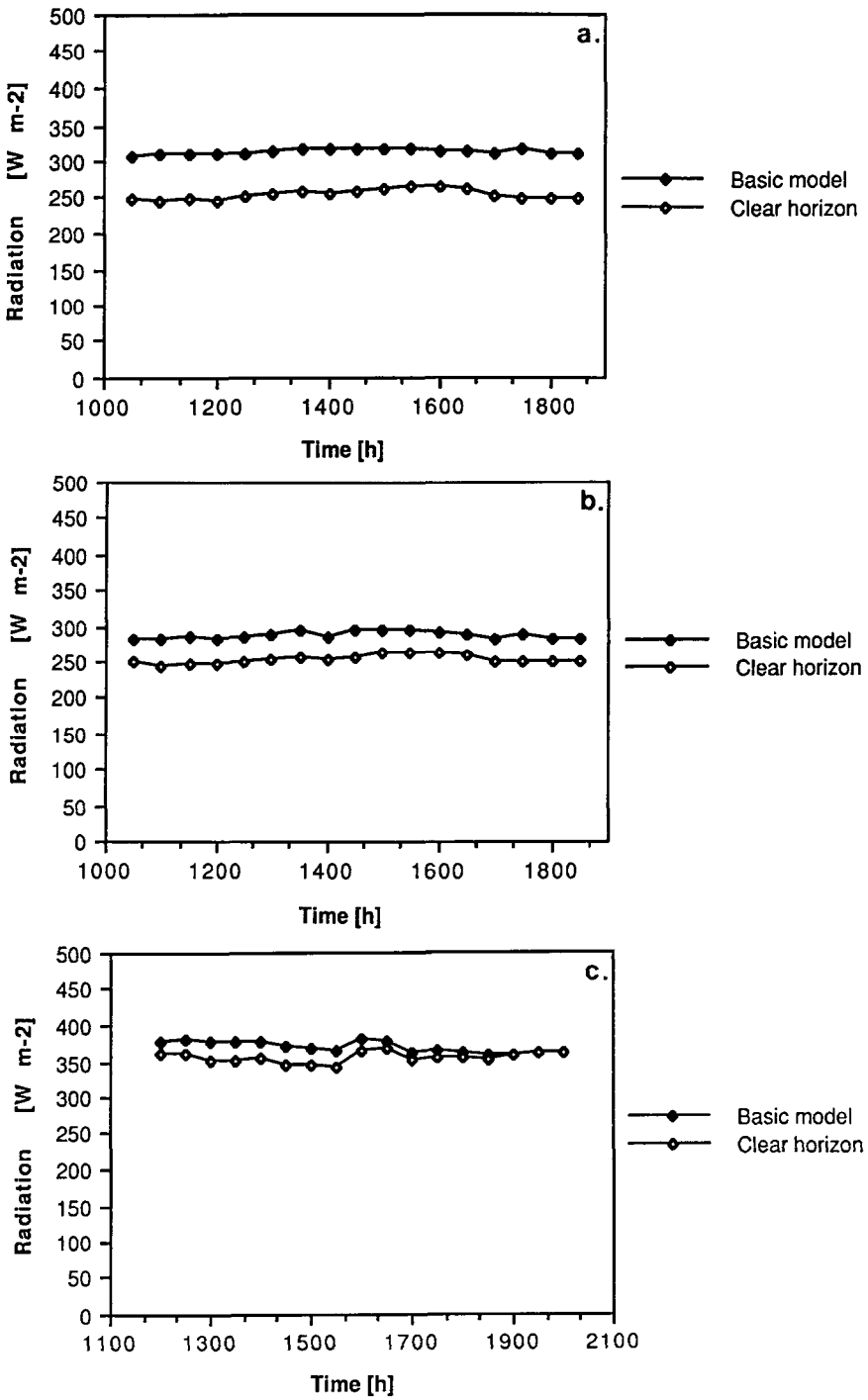

Fig. 2. Incoming clear-sky longwave radiation predicted by the rigorous model and the clear-horizon model for selected walls. (a) Lower east wall, site #1, (b) Upper east wall, site #1, (c) West wall, site #2.

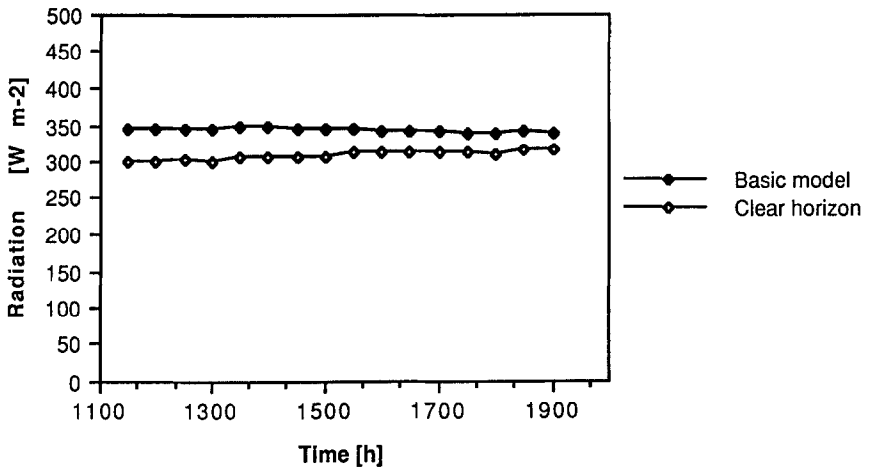

Fig. 3. Incoming cloudy-sky longwave radiation predicted by the rigorous model and the clear-horizon model for the lower east wall at site #1.

May; wall-sky temperature differences are therefore larger at site 1 due to the strong internal heating of buildings (and the fact that the walls were poorly insulated). At site 2, rapid cooling to air temperature occurred after sunset because of the large sky view factor of the floor of the enclosure; at site 1, the enclosure floor not only had a small sky view factor, but was also heated from below.

The results of the remaining simplifying assumptions are illustrated for selected walls, under clear and cloudy conditions, in Figures 4 and 5, respectively. Predictions of simplified versions of the model are presented as deviations from those of the rigorous model.

The assumption of an isotropic sky can be expected in general to lead to an underestimation of incoming longwave radiation on vertical walls, because the intensity of sky longwave radiation characteristically varies from a maximum at the horizon to a minimum at the zenith, and vertical walls usually have a larger view of sky at high zenith angles than at low zenith angles. For clear skies, underestimations averaging 2–3 $W m^{-2}$ are indeed found on the upper walls at site 1 and on the walls at site 2. On the lower walls, however, slight overestimations are the rule, because the small portion of sky viewed by these subareas is within the sector of overestimation. Under overcast skies, at site 2 the magnitude of error is marginally larger due to the greater intensity of sky radiation under clouds; at site 1, on the other hand, errors are zero because the ratio of zenith to total hemispheric sky radiation was measured on this day as being almost equal to 1.

The neglect of absorption and emission by the enclosure air leads to overestimations of incoming longwave radiation, because of the fact that the air is

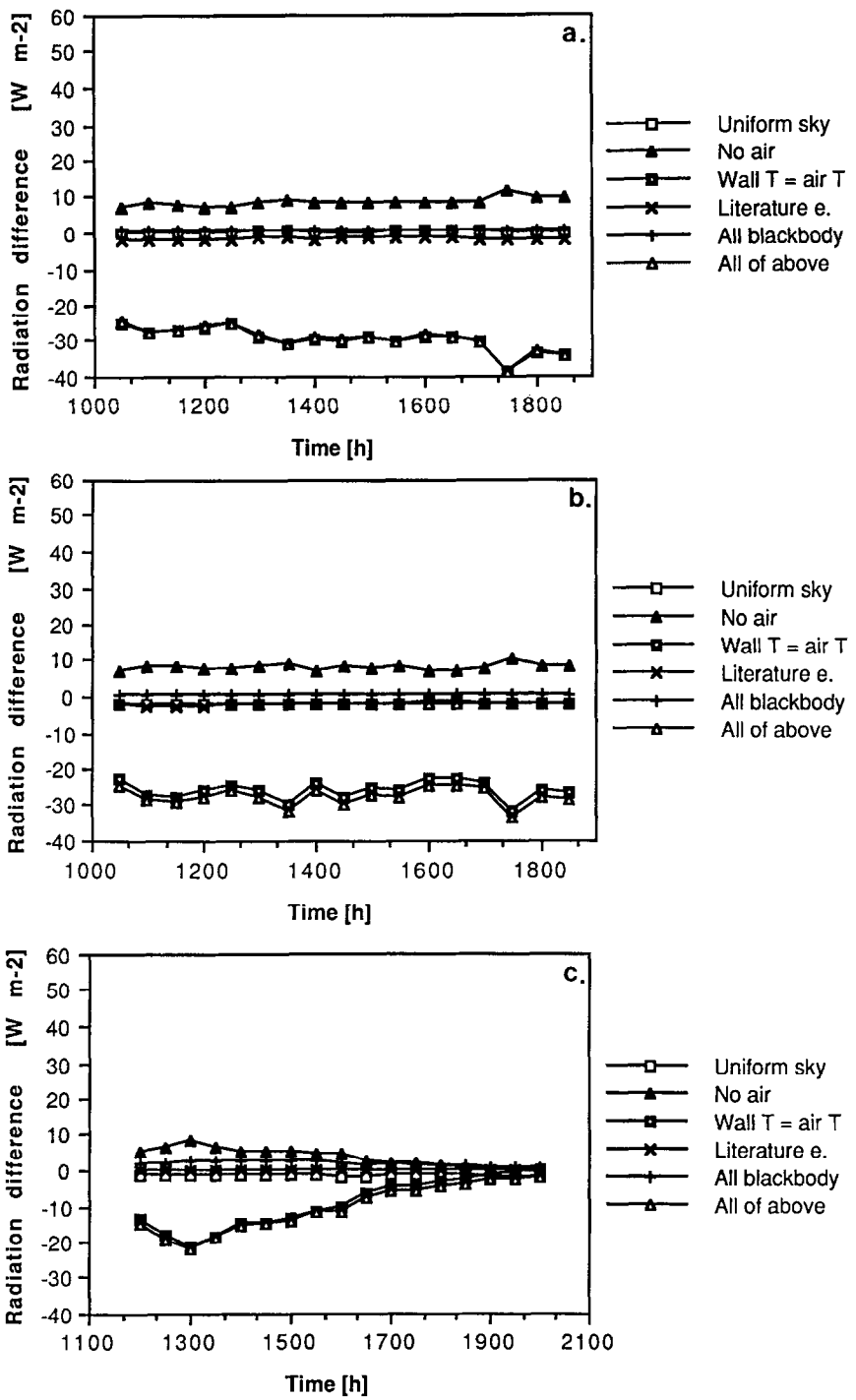

Fig. 4. Incoming clear-sky longwave radiation predictions made by simplified versions of the model compared to predictions of the rigorous model for selected walls. (a) Lower east wall, site #1, (b) Upper east wall, site #1, (c) West wall, site #2.

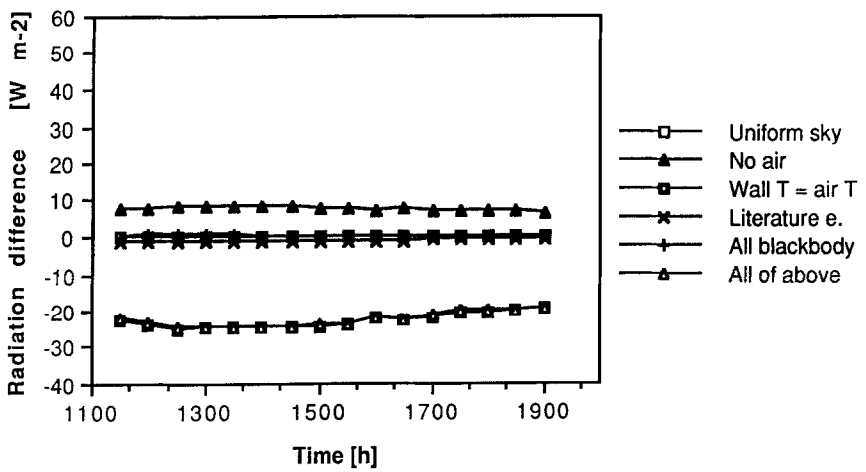

Fig. 5. Incoming cloudy-sky longwave radiation predictions made by simplified versions of the model compared to predictions of the rigorous model for the lower east wall at site #1.

colder than the walls on each of the days of measurement. At site 1, errors average 8 and 9 W m^{-2} under clear skies at the upper and lower walls, respectively; the magnitudes of error are similar because although the upper subareas have larger views of adjacent sunlit walls, the lower subareas have larger views of the heated floor of the enclosure. On the overcast day, errors are almost unchanged for the lower walls, averaging 7 W m^{-2}, but smaller for the upper walls, averaging 4 W m^{-2}, because the upper, exposed levels are closer to ambient air temperature in the absence of direct solar radiation. At site 2, overestimations are small under clear conditions, averaging 4 W m^{-2}; as noted above, the enclosure is closer to air temperature than at site 1, due to the higher sky view factors of the walls and floor and the virtual absence of internal heating of walls. Errors are larger under cloudy conditions, averaging 7 W m^{-2}, because of the fact that the day under study was at first partly cloudy and then overcast. The walls were therefore heated by direct solar radiation for the first part of the day, and the cloud cover subsequently inhibited radiative cooling after sunset.

If air temperatures are generally lower than wall temperatures, the assumption of wall and ground temperatures equal to air temperatures must lead to underestimation of incoming longwave radiation. At site 1, the lower walls and the floor of the enclosure are considerably warmer than the enclosure air under both clear and cloudy conditions, due to internal heating and little exposure to the cold sky; the magnitude of the error for the lower walls therefore averages 30 W m^{-2} under clear and 23 W m^{-2} under cloudy conditions. The upper walls view sunlit walls under clear conditions, causing errors of similar magnitude averaging 25 W m^{-2}; under cloudy conditions, the lower temperatures of the walls viewed lead to errors averaging 13 W m^{-2}. At site 2, the smaller wall-air temperature difference leads to a relatively small average error of 8 W m^{-2} under

clear skies. Under partly cloudy to overcast skies, rapid heating during the first half of the day followed by slow cooling leads to larger errors averaging $13\ W\ m^{-2}$.

Finally, the use of published values of emissivities and the assumption of black body surfaces will be considered concurrently. Referring to Table I, it can be seen that the emissivities of the surfaces under study are generally slightly higher than the values obtained from the literature. It therefore follows that the use of published values of emissivities will lead to underestimations of incoming longwave radiation, due to the larger fraction of sky longwave radiation reflected from walls. The use of the black body assumption, on the other hand, must lead to overestimation of incoming radiation due to the absence of reflected sky radiation. However, from Tables IV and V it is evident that these errors are negligible. At site 1, where wall view factors are greatest, the underestimations due to the use of published values of emissivities do not exceed $2\ W\ m^{-2}$ under both clear and cloudy conditions. At site 2, the errors approach zero. In the case of the black body assumption, errors only reach $2\ W\ m^{-2}$ at site 2, where emissivities are lowest, and then only under clear skies. In all other cases, the magnitude of error is less than $1\ W\ m^{-2}$.

6. Conclusions

The model developed in Verseghy and Munro (1989) to calculate the shortwave radiation incident on surfaces in a building enclosure has been extended to the case of incident longwave radiation. The locations of horizon obstructions, the emissivities and temperatures of enclosure surfaces, the angular distribution of sky radiation and the effects of absorption and emission by enclosure air are accounted for. Field measurements collected at two sites under clear and cloudy conditions are used to test the model; it is found that the root-mean-square errors associated with model predictions are of the order of $10\ W\ m^{-2}$.

The effects of several simplifying assumptions are investigated. Neglect of horizon obstructions causes the most serious errors, averaging $60\ W\ m^{-2}$ in the worst case. The assumption of wall temperatures equal to air temperatures results in the next most severe errors, ranging up to $35\ W\ m^{-2}$. Errors associated with neglect of absorption and emission by the enclosure air reach averages of $10\ W\ m^{-2}$. The other simplifying assumptions tested include the assumption of sky isotropy, the use of emissivities obtained from the literature rather than those measured *in situ*, and the black body surface assumption. These all cause negligible errors, not exceeding $5\ W\ m^{-2}$ in the worst case.

From the above results, it can be concluded that only the neglect of horizon obstructions, the assumption of wall temperatures equal to air temperatures, and possibly the neglect of air absorption and emission between walls lead to errors equalling or exceeding those associated with the predictions of the rigorous model itself. As pointed out in our earlier paper, these conclusions strictly

speaking apply only to walls in the same situation and modelled at the same time of year as in the present study. It is, however, demonstrated that as in the shortwave case, care must be exercised in simplifying a model intended to calculate the longwave radiation incident on urban surfaces.

Acknowledgment

The first author gratefully acknowledges the support provided by a Canada Mortgage and Housing Corporation Postgraduate Scholarship during the period of research.

References

ASHRAE: 1977, *Handbook of Fundamentals*, American Society of Heating, Refrigerating and Air-Conditioning Engineers, New York, 756 pp.

Arnfield, A. J.: 1976, 'Numerical Modelling of Urban Surface Radiative Parameters', in *Papers in Climatology – The Cam Allen Memorial Volume*, McMaster University, Hamilton, Canada, 141 pp.

Buettner, K. J. K. and Kern, C. J.: 1965, 'The Determination of Infrared Emissivities of Terrestrial Surfaces', *J. Geophys. Res.* **70**, 1329–1337.

Cole, R. J.: 1979, 'The Longwave Radiation Incident upon Inclined Surfaces', *Solar Energy* **22**, 459–462.

Hare, F. K. and Thomas, M. K.: 1979, *Climate Canada*, Wiley, Toronto, 230 pp.

Kondratyev, K. Ya.: 1969, *Radiation in the Atmosphere*, Academic Press, New York, 912 pp.

Martin, M. and Berdahl, P.: 1984, 'Summary of Results from the Spectral and Angular Sky Radiation Measurement Program', *Solar Energy* **33**, 241–252.

Oke, T. R.: 1978, *Boundary-Layer Climates*, Methuen, London, 372 pp.

Oke, T. R.: 1982, 'The Energetic Basis of the Urban Heat Island', *Quart. J. Roy. Meteorol. Soc.* **108**, 1–24.

Sellers, W. D.: 1965, *Physical Climatology*, University of Chicago Press, Chicago, 272 pp.

Siegel, R. and Howell, J. R.: 1981, *Thermal Radiation Heat Transfer*, McGraw-Hill, New York, 862 pp.

Staley, D. O. and Jurica, G. M.: 1970, 'Flux Emissivity Tables for Water Vapour, Carbon Dioxide and Ozone', *J. Appl. Meteorol.* **9**, 365–372.

Sutherland, R. A. and Bartholic, J. F.: 1977, 'Significance of Vegetation in Interpreting Thermal Radiation from a Terrestrial Surface', *J. Appl. Meteorol.* **16**, 759–763.

Todhunter, P. E. and Terjung, W. H.: 1988, 'Intercomparison of Three Urban Climate Models', *Boundary-Layer Meteorol.* **42**, 181–205.

Unsworth, M. H. and Monteith, J. L.: 1975, 'Long-wave Radiation at the Ground: I. Angular Distribution of Incoming Radiation', *Quart. J. Roy. Meteorol. Soc.* **101**, 13–24.

Verseghy, D. L.: 1987, 'On the Measurement and Modelling of Radiative Exchange for Building Surfaces', unpublished Ph.D thesis, University of Toronto, Toronto, 170 pp.

Verseghy, D. L. and Munro, D. S.: 1989, 'Sensitivity Studies on the Calculation of the Radiation Balance of Urban Surfaces: I. Shortwave Radiation', *Boundary-Layer Meteorol.* **46**, 343–365.